ELSEVIER

Chemical Engineering Journal 82 (2001) 157–172

Chemical Engineering Journal

www.elsevier.com/locate/cej

Fundamental and environmental aspects of landfill gas utilization for power generation

W. Qin [a], F.N. Egolfopoulos [b], T.T. Tsotsis [a,*]

[a] *Department of Chemical Engineering, University of Southern California, Los Angeles, CA 90089, USA*

[b] *Department of Aerospace & Mechanical Engineering, University of Southern California, Los Angeles, CA 90089, USA*

Received 26 May 2000; accepted 19 October 2000

Abstract

Landfill gas (LFG) results from the biological decomposition of municipal waste and consists of mostly equal amounts of CO_2 and CH_4, as well as trace amounts of a variety of other organic compounds. Upon removal of most of the trace organic compounds, LFG can be used as fuel in internal combustion engines and gas turbines for generation of heat and electricity. Producing energy from LFG has the additional benefit of preventing its release into the atmosphere, where it results into significant air pollution. The large quantity of CO_2 in landfill gas (typically 40–50%) presents problems with its utilization for energy production, since it negatively impacts combustion efficiency and stability. To improve the economics of LFG utilization for energy production, it is important to develop a better fundamental knowledge base about its burning characteristics. This has been the goal of this combined experimental and numerical investigation. Laminar flame speeds, extinction strain rates, temperature, and species concentrations profiles, including NO_x, were experimentally determined. We have used a stagnation-flow experimental configuration, which makes it possible to simulate the experiments using a complete description of molecular transport and the detailed GRI 2.11 chemical kinetic mechanism. The experimental results from laminar flame speeds, extinction strain rates, species structure, and thermal structures compare generally well with the simulation results. As expected, it was found that the presence of CO_2 in LFG significantly decreases the laminar flame speeds and extinction strain rates. The study indicates that increased CO_2 concentrations in LFG increase the amount of NO emissions per gram of consumed CH_4. Considering a number of detailed (DRM) and semi-detailed radiation models (SRM), we also assessed the effect of thermal radiation on laminar flame speeds, extinction strain rates, and flame structure. The optically thick (DRM) model resulted in higher laminar flame speeds, extinction strain rates, and maximum flame temperatures compared to the optically thin (SRM) model. Fundamental flammability limits were also calculated, and it was found that as the CO_2 concentration increases, the flammable range noticeably decreases. Analysis of the flame structure revealed that the effect of CO_2 on the flame response is of thermal rather than kinetic nature.

Keywords: Landfill gas; GRI 2.11 chemical kinetic mechanism; DRM

1. Introduction

Landfill gas (LFG) is a flammable and potentially harmful gaseous mixture consisting mostly of CH_4 and CO_2 together with trace amounts of a number of volatile organic compounds (VOC). LFG results from the anaerobic decomposition of municipal solid waste (MSW) that is deposited in landfills. Gas production typically starts immediately after the MSW deposition and attains its peak production rate in about 10 years; it can last for up to 40 years or longer after initial deposition. The use of LFG for generating electricity and heat is a promising approach both in terms of conserving energy and also for reducing air pollution. LFG has the potential of becoming a quite abundant and stable source of energy. One ton of MSW, for example, can produce up to $300\,m^3$ of LFG. Though, some of this gas is inadvertedly lost to the atmosphere as fugitive emissions, using current technology a significant fraction of it is also collected.

High grade LFG, typically utilized for electricity production, is mostly composed of CH_4 and CO_2, with some smaller amounts of oxygen and nitrogen. It also contains a large number of trace constituents, some of them halogenated and organosulfur compounds [1]. During utilization of LFG for energy production, these compounds are often removed before the LFG enters the combustion chamber, as they cause corrosion to the combustion equipment and associated hardware. Our group has been actively involved in the development of LFG clean-up technology [2]. LFG, if not properly collected and utilized, can potentially be a significant source of pollution. It can migrate underground and contaminate the ground water resources. As fugitive

* Corresponding author. Tel.: +1-213-740-2069; fax: +1-213-740-8053.
E-mail address: tsotsis@usc.edu (T.T. Tsotsis).

1385-8947/01/$ – see front matter
PII: S1385-8947(00)00366-1

emissions above ground it can potentially create a variety of problems, including odors, destruction of vegetation, and occasional fires and explosions. A more serious problem relates to the fact that both its main constituents (CH_4 and CO_2) are greenhouse gases. EPA estimates show that in 1990, landfills released 25–40 million metric tonnes of methane, and that LFG as a result constitutes about 15% of man-made emissions [3].

The potential detrimental effects of LFG on the environment have been recognized, and regulations have been issued limiting its release through the use of various gas control measures. In the majority of landfills today, the gas that is collected is flared at the site. It was only in the late 1980s that it was first realized that LFG could be exploited as a fuel, thus providing a potential source of revenue, reducing fossil fuel use in addition to implementing the key objective of environmental protection [4]. Since then, a number of efforts have been undertaken looking for environmentally friendly ways to control and exploit the large amounts of LFG that are currently available. Power generation from LFG is still at an early stage of development, and not yet, for the most part, commercially competitive at today's electricity prices. It could, however, become fully commercial under tighter environmental protection standards, requiring that the landfill sites collect LFG for energy generation in front of which is the most plausible future alternative to flaring.

Typically, LFG is a low-BTU gas, but on the average, its total chemical energy is sufficient to sustain the operation of a gas turbine, and to serve as a basis for the production of heat and electricity. Given the large fraction of CO_2 found in LFG, its combustion characteristics are different from those of natural gas (NG), since the presence of CO_2 results in reduced flame temperatures and burning rates, a narrower range of flame stability, and thus lower combustion efficiency. One approach to solving these problems is through thermal energy recuperation of the combustion product gases in order to heat the reactants, and thus increase the temperature in the reaction zone. In doing so, one improves the burning characteristics of low-BTU fuels like LFG. This is an area of current research interest by our group [5]. The practical limitations of this approach lie in the cost and maintenance of the complicated combustion systems needed. Another approach is to raise the heating value of LFG through addition of a higher-grade fuel or by burning the gas in two-stage systems, where a higher calorific value gas is used for flame stabilization. Combustors of this type are popular in industrial applications, especially in processes, where the amount and composition of the LFG are variable. However, the higher the fraction of high-grade fuel addition is, the lower are the savings realized.

The efficient combustion of LFG will certainly benefit by a better fundamental understanding of the effect of CO_2 on fundamental flame properties. Though, in the literature a large number of experimental measurements for CH_4/air mixtures exist, systematic studies on the effect of CO_2 on burning rates, extinction, and pollutant formation are limited. These past studies either focused on the effect of CO_2 on the flammability limits (e.g. [6,7]), as CO_2 can effectively radiate and reabsorb thermal energy, or on its effect on laminar flame speeds (e.g. [8]). No study, however, has provided a comprehensive data base on the effect of CO_2 on flame propagation, extinction, structure, and pollutant emissions.

In view of these considerations, the main objective of this study is to provide a comprehensive understanding of LFG combustion through a combined experimental and detailed numerical investigation. The study was conducted for simulated LFG by varying the CO_2 mole fraction in the fuel feed, X_{CO_2}, from 0 to 50%, a typical range under realistic conditions. Experiments included the determination of laminar flame speeds, extinction strain rates, stable species and NO_x concentrations, and thermal flame structures. The numerical simulations of the experiments included the use of detailed description of chemical kinetics and molecular transport.

2. Experimental approach

The experiments were conducted for fuel-lean mixtures, using the stagnation-flow experimental configuration (e.g. [9,10]) in which a planar flame is established between a nozzle and a variable temperature plate that acts as the stagnation plane. The velocity profile measured along the system centerline has a near zero gradient at the nozzle exit, and gradually develops an increasing slope, which reaches its maximum just before the minimum velocity point where heating starts. This maximum velocity gradient in the hydrodynamic zone is defined as the imposed aerodynamic strain rate, K, and the minimum velocity as a reference upstream flame speed, $S_{u,ref}$. For a given mixture, the variation of $S_{u,ref}$ with K is plotted, and by linearly extrapolating the value of $S_{u,ref}$ to $K = 0$, the laminar flame speed, S_u^o, is determined as the intercept on the ordinate [10–13]. The values of the experimentally determined S_u^o are not affected by the presence of the non-adiabatic plate, as it has been shown in a previous study [14]. As the strain rate increases, extinction occurs at a critical value K_{ext}.

The axial flow velocities were measured using laser Doppler velocimetry (LDV) by seeding the flow with 0.3 μm Al_2O_3 particles, small enough to follow the gas phase closely, while efficiently scattering the laser light. The spatial step utilized for measuring the axial profile along the centerline of flow was within the range of 0.01–0.1 mm.

The thermal structures were measured by using fine-wire thermocouples, similar to previous studies [15–18]. Care was taken in order to minimize disturbances that can be of aerodynamic, thermal, and chemical nature (e.g. [19,20]). Aerodynamic disturbances are the most serious but can be eliminated in streaming flows without creating a zone of flow reversal, through the use of the appropriate thermocouple geometry. Other thermocouple-induced interference may result from chemical reactions on the wire surface. Coating the wires with a suitable non-reactive material

minimized chemical interactions. A combination of beryllium and yttrium oxide was used as a ceramic coating for the thermocouples. This coating has been found [21] to be stable, easy to apply, impermeable to flame gases, and non-reactive in a typical flame environment. Systematic errors due to radiation effects have been estimated and compensated for through energy balance on the thermocouple junction, similar to previous investigations (e.g. [22,23]).

The spatial variations of stable species concentrations were determined through direct micro-probe gas sampling followed by molecular beam mass spectrometry (MBMS) analysis; carbon monoxide (CO) could not be measured using MBMS. The accuracy of the measurements is limited by the spatial resolution that can be achieved by the micro-probe. A water-cooled, aerodynamically quenching quartz micro-probe was used with an orifice diameter of about 50 μm. The micro-probe was appropriately positioned to extract samples from the centerline of the flame. Careful design, guided by the relationship between characteristic length scales of the probe and the flames, minimized the disturbance of the scalar concentration gradients in the vicinity of the probe due to the streamline distortion, as manifested by the repeatability of the experimental data. For the analysis of stable species, the sampling line was maintained at 2 Torr, and a small portion of the sample was led to the mass spectrometer chamber through a pinhole. The sample then would pass into a second chamber through a skimmer to form a pseudo-molecular beam. The beam was chopped to provide background discrimination and was focused onto the ionizer region of the quadrupole mass spectrometer. The ion signals were detected with a locked-in amplifier. Calibration of the mass spectrometer was achieved by determining the relative sensitivities. Quantitative species profiles were obtained by correcting the ion signal for mass species interference, then combining the sensitivities relative to each other with the corrected peak intensities to obtain ratios of mole fractions of the species.

The NO_x concentration measurements were carried out by sampling with a micro-probe that is similar to the one used with the MBMS, and the subsequent use of a chemiluminescence NO_x analyzer. A Teflon tube leads the sample to the analyzer reactor. Both the micro-probe and the Teflon tube are heated so that water condensation is avoided; the presence of liquid water may falsify the results as NO_x can dissolve in it.

3. Numerical approach

The experimental results on extinction and flame structure were modeled using a one-dimensional (1D) code (e.g. [24]) that integrates the full, steady state conservation equations of mass, momentum, energy, and species along the stagnation streamline. The laminar flame speeds and the fundamental flammability limits were calculated using the 1D Premix code of Kee et al. [25]. Both codes were modified to include thermal radiation for CH_4, CO, CO_2, and H_2O, and a one-point continuation approach was implemented allowing for the description of the reacting configuration around singular extinction points.

In our previous studies (e.g. [24]), the strain rate was determined as a result of the independently imposed nozzle exit velocities. The stagnation-flow code was modified and a one-point continuation approach was implemented by imposing a pre-determined temperature reduction at one point within the flow field, so that the nozzle exit velocity (strain rate) would become part of the solution, and its respective boundary value was removed. The inner point was chosen to be the location at which the temperature profile has a maximum slope [26]. The fundamental flammability limits were obtained by modifying the 1D Premix code [25] in order to capture the turning-point behavior in the equivalence ratio domain. This was achieved by introducing a one-point continuation approach similar to the one described for the stagnation flow code. The only difference is that in the Premix code, the free-stream fuel concentration would now become part of the solution and its respective boundary value was removed. The mathematical details of the one-point continuation are described in detail by Nishioka et al. [26].

Two models of radiative heat transfer were used. The first, termed the simple radiation model (SRM), included the use of the Planck's mean absorption coefficient, and the assumption of an optically thin gas. Law and Egolfopoulos [27] and Egolfopoulos [28] have explained the details of this formulation, for example. The second, termed the detailed radiation model (DRM), included the use of the subroutine RADCAL [29] that predicts the spectral structure of various combustion products over a wide range of temperature, pressure, and path-length. It solves the equation of transfer for an absorbing and emitting medium (no scattering) by breaking the line-of-sight into a number of uniform elements. It also uses molecular models and tabulated data for spectral absorption coefficients. The RADCAL provides the spectral absorption coefficients for the radiating species of CO_2, H_2O, CO, CH_4, and soot particles. Since lean mixtures were of interest in this study, the soot was not included. SRM and DRM were implemented for both the stagnation flow configuration and the freely propagating flame. The use of DRM was essential given the possibility that reabsorption is important, as CO_2 is present in the unburned gas mixture.

Both codes were integrated with the Chemkin-II [30] and Transport [31] subroutine libraries. The GRI 2.11 [32] mechanism was used for the description of the kinetics, which includes nitrogen chemistry relevant to natural gas combustion and contains 49 species and 277 elementary reversible chemical reactions. The strain rate, K, is determined as the maximum velocity gradient in the hydrodynamic zone just before the flame, similar to its experimental determination.

4. Results and discussion

Measurements and simulations were conducted for fuel-lean mixtures as they are of relevance to practical combustors. All measurements were conducted at atmospheric pressure along the stagnation streamline of the stagnation flow, and for a separation distance between the nozzle exit and the stagnation plane (wall) equal to 16 mm. The simulations of laminar flame speeds, extinction strain rates, flame structures, and flammability limits were computed by employing the SRM in the code. The differences between SRM and DRM are addressed in a later section.

4.1. Laminar flame speeds

The effect of the CO_2 concentration in the fuel mixture on S_u^o can be seen in Fig. 1. The experimentally measured S_u^o (points) are shown together with the results of the numerical simulations (lines) as functions of X_{CO_2} and the equivalence ratio, ϕ; ϕ is defined as the fuel to air ratio divided by its value under stoichiometric conditions. As expected, the results indicate that for the same ϕ, addition of CO_2 to the fuel significantly reduces S_u^o. For example, for a flame with $\phi = 0.75$ when X_{CO_2} varies from 0 to 50%, the value of S_u^o decreases by about 45%. The experimentally measured S_u^o's are, in general, in good agreement with the predicted values. A three-dimensional (3D) plot of simulated S_u^o as a function of X_{CO_2} and ϕ is shown in Fig. 2. Clearly, as X_{CO_2} increases, the flames become weaker and the ability to operate fuel-lean, diminishes. The laboratory results mirror the field experience with IC engines, where the rule of thumb is that LFG containing more than 50% CO_2 is very difficult to use for energy production.

4.2. Flame extinction

Fig. 3 depicts the variation of K_{ext} with X_{CO_2} and ϕ, for a fixed value of the wall temperature, T_{wall}. As it was also observed with the laminar flame speeds, increasing X_{CO_2} results in significant reduction of K_{ext}, pointing out again the detrimental effect that the presence of additional CO_2 has on the fuel's combustion characteristics. For example, the value of K_{ext} for $X_{CO_2} = 50\%$ is only 30% of the value observed for a pure CH_4 flame. This is a relatively larger reduction than that observed for the S_u^o's shown in Fig. 1. The effect of T_{wall} on K_{ext} is shown in Fig. 4 for various values of X_{CO_2} and for $\phi = 0.7$. It can be seen that the higher the T_{wall} is, the greater the experimentally observed and simulated values of K_{ext} are. The dependence of K_{ext} on T_{wall}, however, is not as strong as that on X_{CO_2}. Similar observations of the effect of K_{ext} on T_{wall} were made in a recent study [14]. More specifically, it was shown that flame

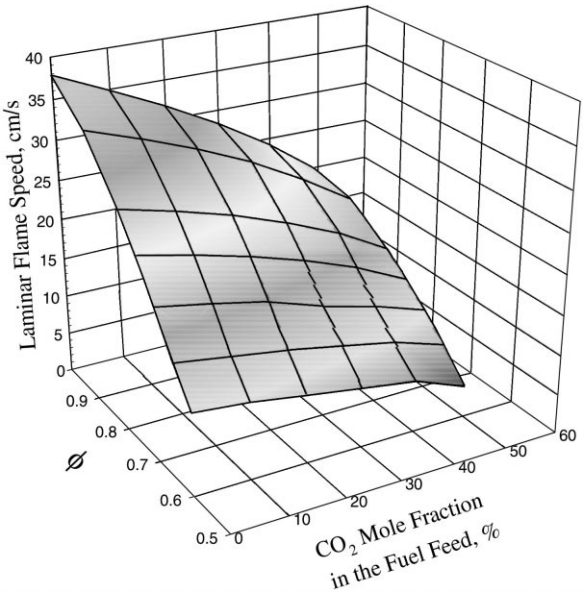

Fig. 2. Variation of the numerically determined laminar flame speeds with CO_2 mole fraction in the fuel feed and equivalence ratio, ϕ, in a 3D view.

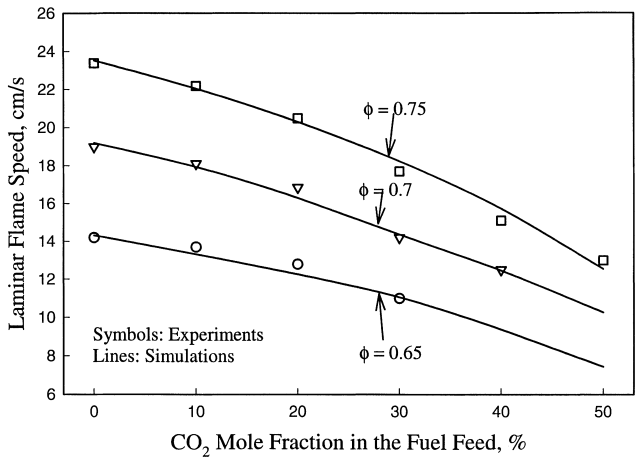

Fig. 1. Experimentally and numerically determined laminar flame speeds as functions of CO_2 mole fraction in the fuel feed and equivalence ratio, ϕ.

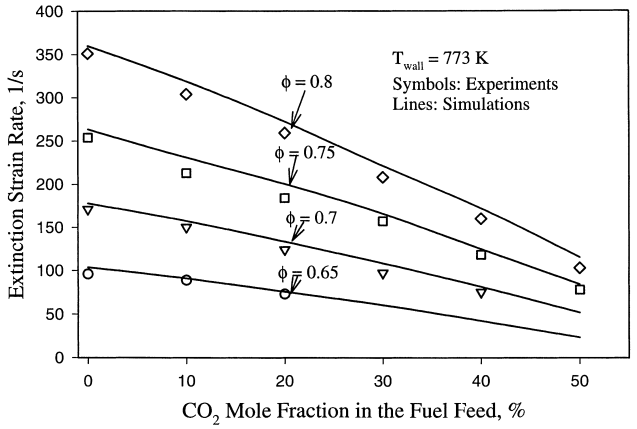

Fig. 3. Experimentally and numerically determined extinction strain rates as functions of CO_2 mole fraction in the fuel feed and equivalence ratio, ϕ.

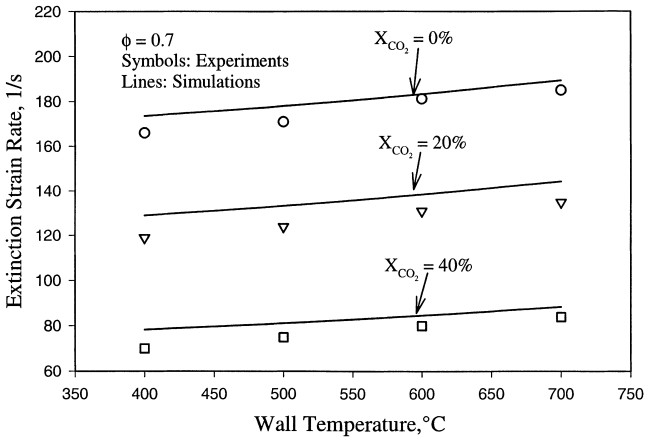

Fig. 4. Variation of experimentally and numerically determined extinction strain rates with wall temperature.

extinction is controlled by the presence of heat loss, and that the magnitude of this heat loss has a secondary effect on the extinction behavior.

Though, simulated results are in qualitative agreement with the experiments, the GRI 2.11 mechanism, which predicts closely the experimental data of S_u^o, does somewhat over-predict the experimentally measured K_{ext} values. This difference in behavior may be explained by the fact that the rate parameters in the GRI 2.11 mechanism were optimized based on its agreement with experimentally reported S_u^o's rather than with K_{ext}'s. Nevertheless, the observed discrepancies are considered as minor, and it is apparent that the GRI 2.11 mechanism describes satisfactorily the fuel-lean oxidation of LFG. This is not surprising, as propagation and extinction are both high-temperature phenomena and their respective controlling kinetic paths are similar. Thus, a mechanism that is optimized on flame speeds is expected to

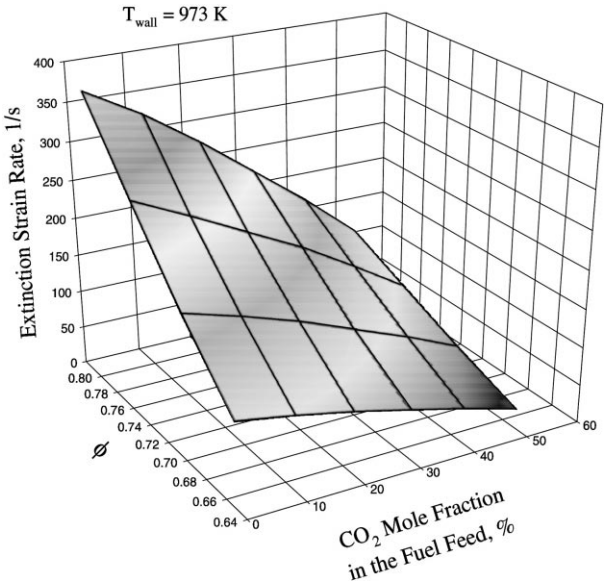

Fig. 5. Variation of numerically determined extinction strain rates with CO_2 mole fraction in the fuel feed and equivalence ratio, ϕ, in a 3D view.

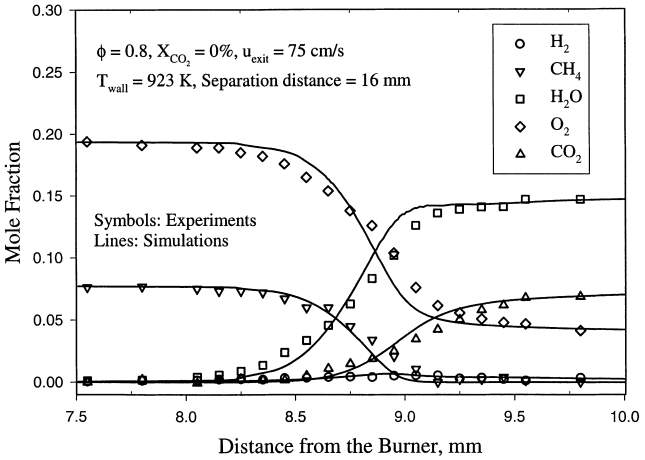

Fig. 6. Spatial variation of experimentally and numerically determined mole fractions of major species.

satisfactorily predict extinction conditions, as has also been shown in a past study [14]. Fig. 5 depicts the dependence of K_{ext} on both X_{CO_2} and ϕ, as predicted by numerical simulations. The detrimental effect of increasing X_{CO_2} and the beneficial effect of increasing ϕ are further demonstrated.

4.3. Flame structure

In order to provide additional insight into the details of the combustion mechanisms of LFG, the concentration profiles of a number of stable species were experimentally and numerically determined for a wide range of conditions. Figs. 6 and 7 depict the variation of the mole fractions of H_2, CH_4, H_2O, O_2, and CO_2 with the distance from the burner for two different flames. Fig. 6 depicts the structure of a methane/air flame ($X_{CO_2} = 0\%$) for $\phi = 0.8$ and a mixture exit velocity, u_{exit}, of 75 cm/s. Fig. 7 depicts the structure of a flame with the same ϕ and u_{exit} but with $X_{CO_2} = 40\%$. It is apparent that the addition of CO_2 to the fuel reduces the flame propagation speed, so that the $X_{CO_2} = 40\%$ flame is closer to the

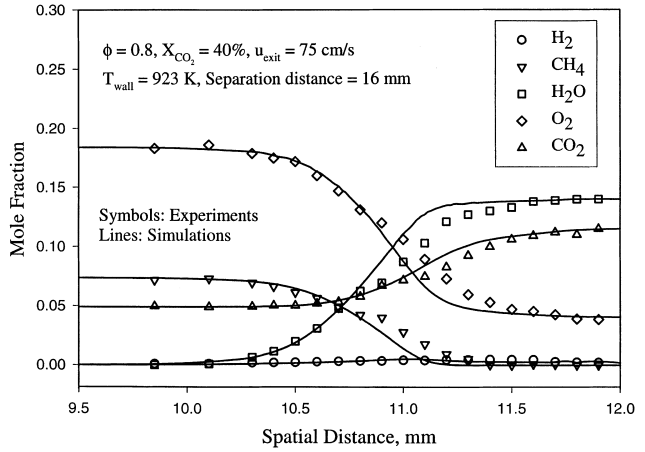

Fig. 7. Spatial variation of experimentally and numerically determined mole fractions of major species.

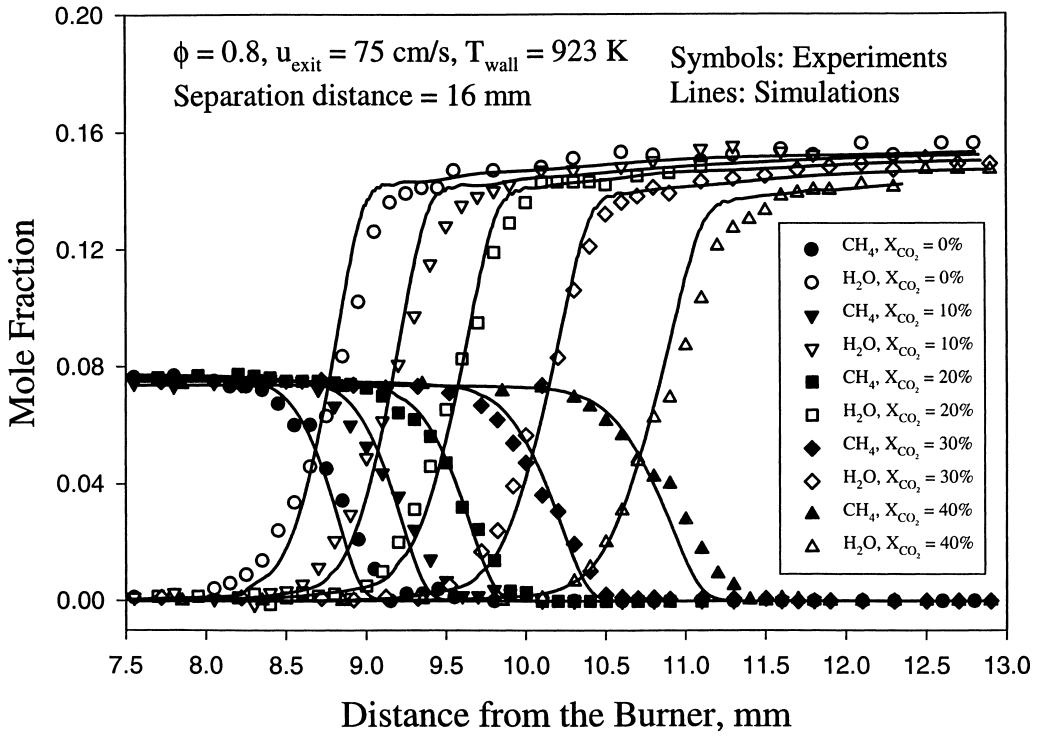

Fig. 8. Spatial variation of experimentally and numerically determined mole fractions of CH_4 and H_2O.

stagnation plane (and further away from the burner) when compared to the pure methane flame for the same u_{exit}. The effect of CO_2 is systematically illustrated in Fig. 8, in which the spatial variations of the CH_4 and H_2O mole fractions are shown for $\phi = 0.8$ and $u_{exit} = 75$ cm/s, and for values of X_{CO_2} ranging from 0 to 40%. The results of Figs. 6–8 suggest that the simulations closely predict the spatial profiles of the stable species before and after the flame. However, there are some noticeable differences within the flame zone.

In order to complement the knowledge of the flame structures gained by composition measurements, extensive experimental investigations of flame thermal structures were also carried out. Fig. 9 depicts a number of temperature profiles for a range of X_{CO_2} values for $\phi = 0.8$ and $u_{exit} = 68.5$ cm/s. As expected, when CO_2 is added to the fuel, the flame moves closer to the wall and the flame temperature drops. Fig. 10 depicts a number of thermal structures for a range of u_{exit} with $\phi = 0.8$ and $X_{CO_2} = 0\%$. While the flame moves toward the wall as the strain rate increases, the flame temperature does not change to the extent that results from CO_2 addition. Shown on the same figures are the simulated temperature profiles. Similar to the stable species structure studies, minor discrepancies between experiments and simulations can be seen, especially for the higher X_{CO_2} values, as shown in Fig. 9.

4.4. Flammability limits

Fundamental flammability limits were determined by using the modified Premix code and by identifying turning points in the equivalence ratio domain. These turning points indicate the concentration limits beyond which propagation is not possible, and their existence is caused by the presence of thermal radiation. The simulations were conducted by using the SRM for different values of X_{CO_2} and various pressures. Fig. 11 depicts the variation of S_u^o with ϕ at 1 atm pressure, and for X_{CO_2} varying from 0 to 60%. It is apparent that as X_{CO_2} increases, the flammable range noticeably decreases and the value of S_u^o is reduced for the same ϕ. Fig. 12 depicts the effect of pressure for $X_{CO_2} = 0\%$, and it can be seen that as the pressure increases, both the lean and rich flammability limits increase, resulting thus to a shift of the flammable range towards higher ϕ values in agreement with previous studies (e.g. [27]). This difference between the two limits can be traced to the different chain mechanisms that are competing on the lean and the rich side. While on the lean side the main termination reaction is a three-body one, on the rich side it is a two-body one [27,33].

4.5. Effect of radiation model

The effect of the various radiation models on the flame structure and dynamic response was tested through simulations using both the SRM and DRM. This test was necessary as the presence of CO_2 can result in energy reabsorption that can, in turn, alter the thermal state of the unburned mixture, as it has been noted by Ju et al. [7]. Radiation heat loss affects the flame temperature, laminar flame speeds, extinction strain rates, and NO_x production. Furthermore, it is

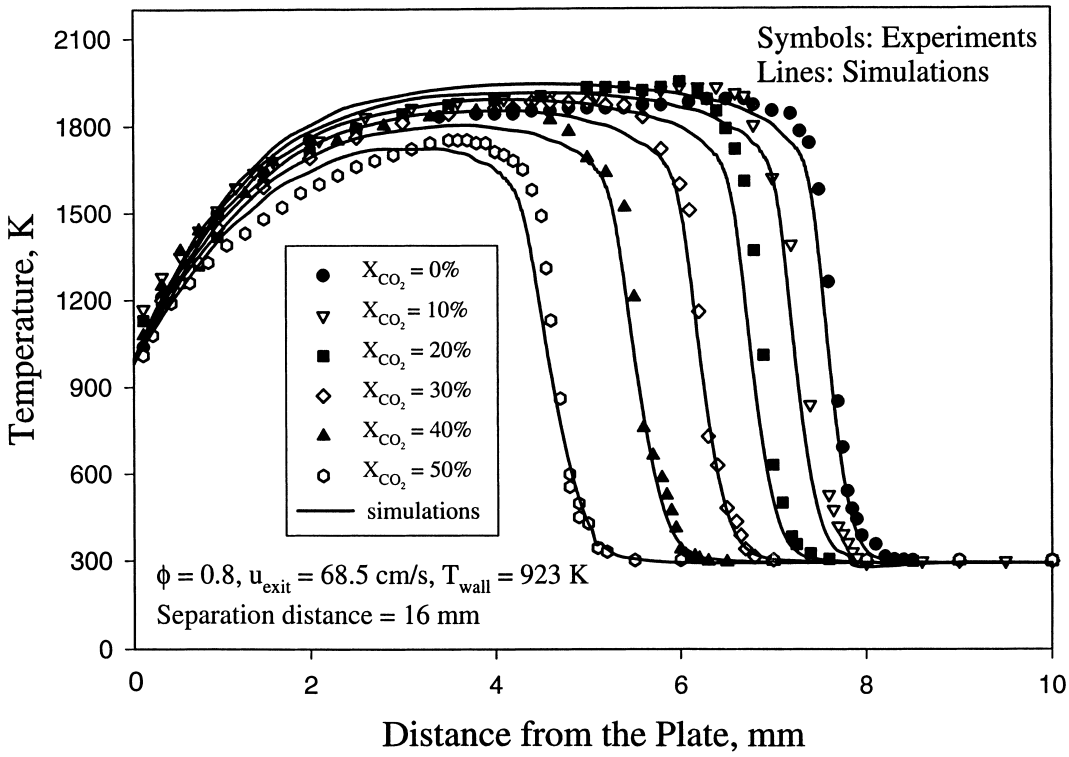

Fig. 9. Spatial variation of experimentally and numerically determined flame temperatures along the stagnation streamline.

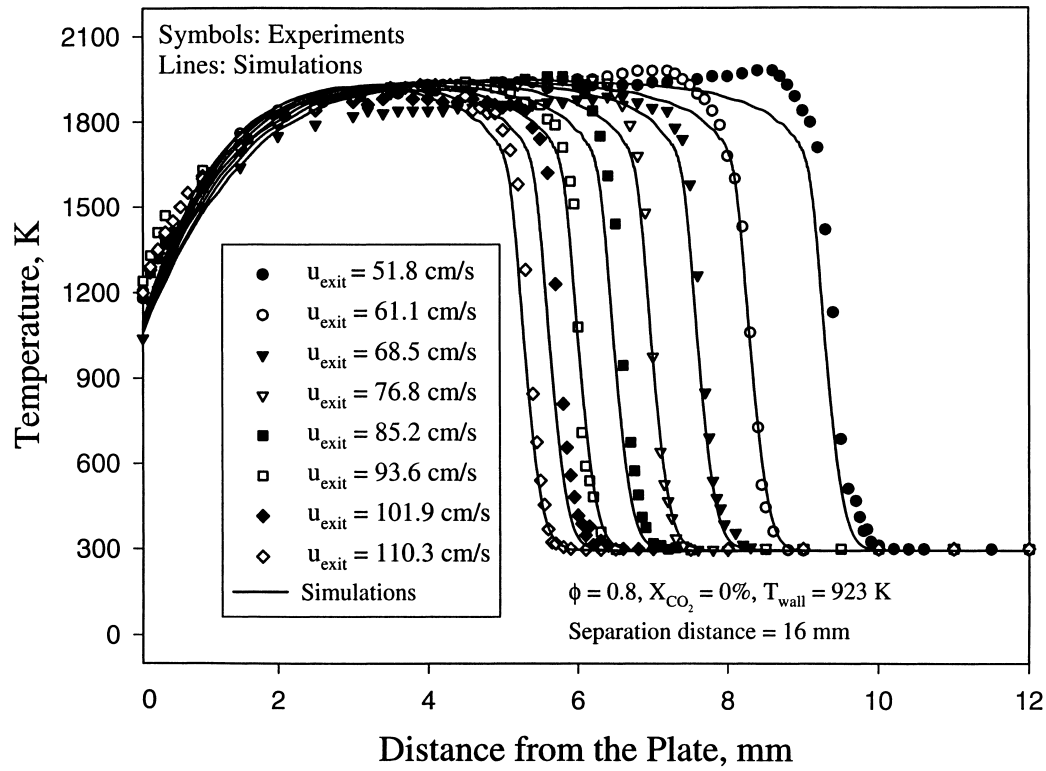

Fig. 10. Experimentally and numerically determined flame temperature profiles along the stagnation streamline.

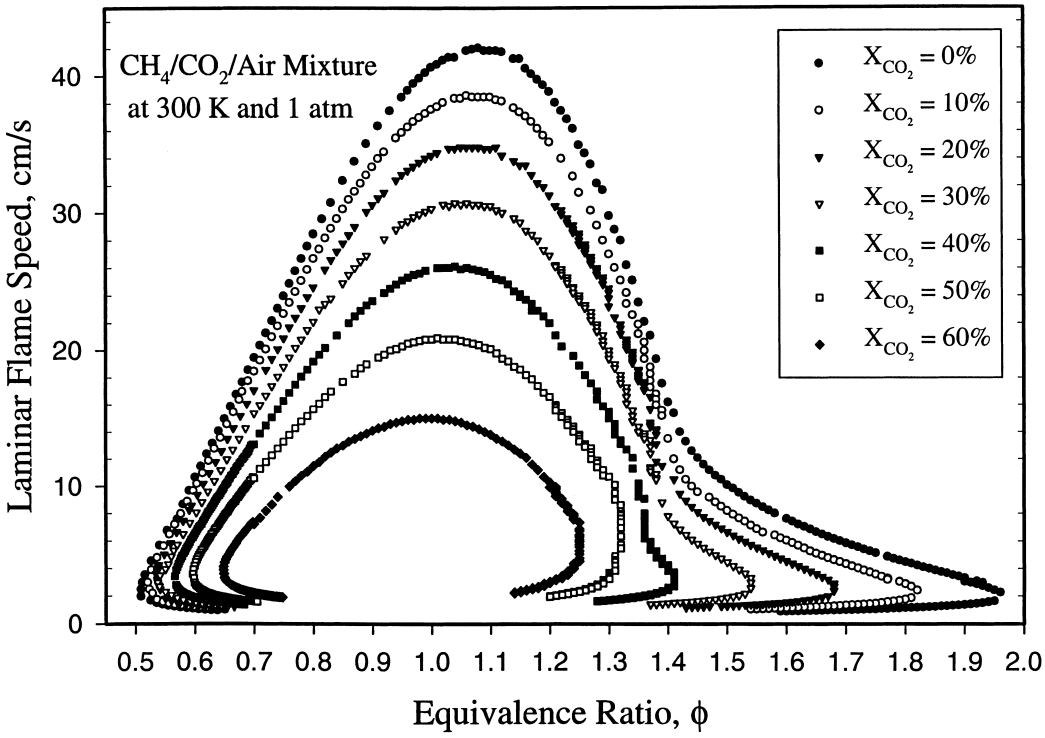

Fig. 11. Numerically determined flammability limits of CH_4/CO_2/air mixtures as functions of the CO_2 mole fraction in the fuel feed, using SRM.

responsible for the existence of fundamental flammability limits. Reabsorption is important as it can reduce the extent of the net radiative loss from the system, and this can have a noticeable effect on near-limit flames [6]. Thus, the DRM was incorporated into the flame codes by accounting for the wavelength dependence and reabsorption. Zhang and Egolfopoulos [34] further describe details of the implementation of the DRM into the flame codes.

The DRM was implemented in modeling 1D freely propagating atmospheric methane/air/CO_2 flames for CO_2 concentrations varying from 0 to 50%. In order to test the validity of the assumption of the optically thin model, the same conditions were simulated by SRM and also compared with the adiabatic case. Fig. 13 depicts the predicted maximum flame temperatures calculated for adiabatic conditions as well as using the SRM and DRM. The adiabatic flame temperatures are above the temperatures calculated using the SRM for the entire range of CO_2 concentration. The difference increases from 30 to 50 K when the X_{CO_2} changes from 0 to 50%. The SRM ignores the reabsorption, so that there

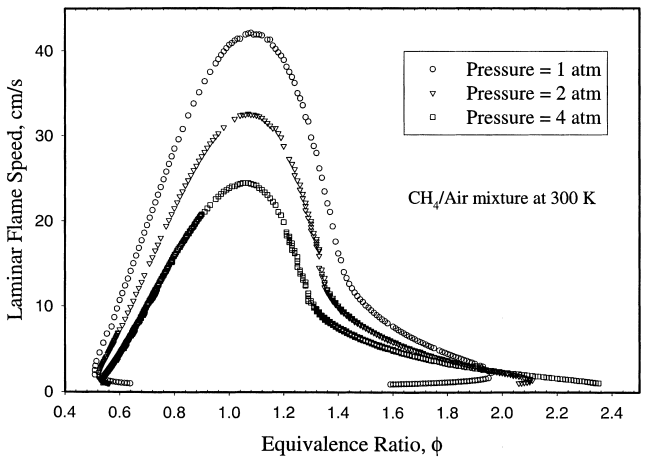

Fig. 12. Numerically determined flammability limits of CH_4/CO_2/air mixtures as functions of pressure, using SRM.

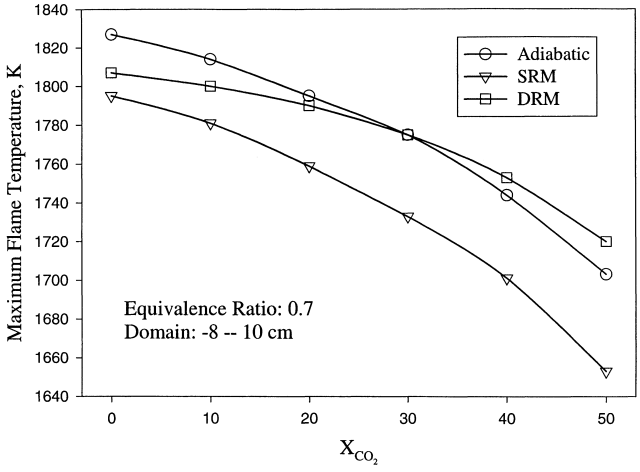

Fig. 13. Variation of the maximum flame temperature with the CO_2 mole fraction in the fuel feed, using the adiabatic assumption as well as SRM and DRM.

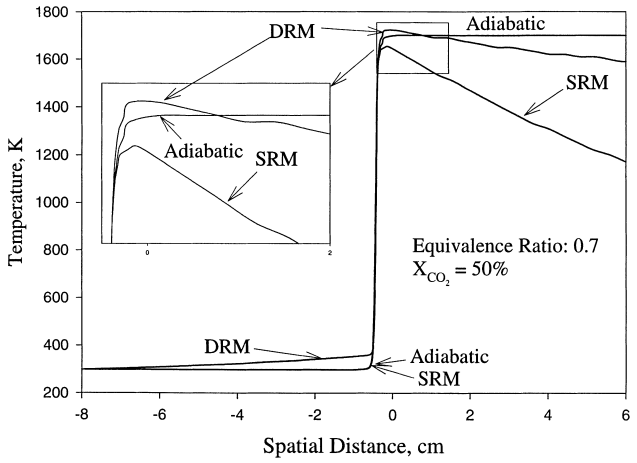

Fig. 14. Temperature profiles of 1D freely-propagating flames, using the adiabatic assumption as well as SRM and DRM.

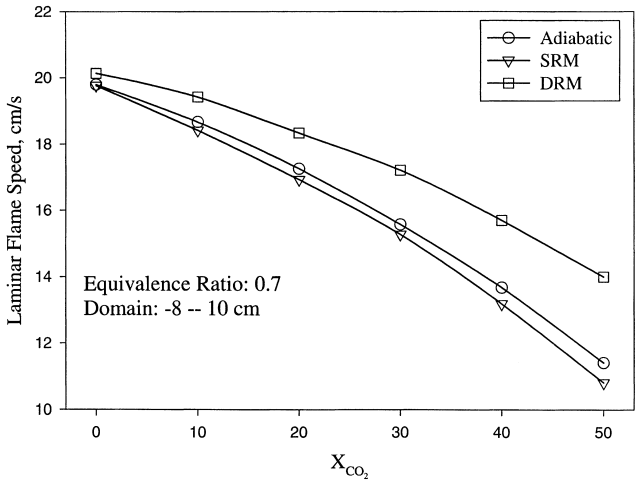

Fig. 15. Laminar flame speeds as functions of CO_2 mole fraction in the fuel feed, using the adiabatic assumption as well as SRM and DRM.

is a net heat loss from the flame, causing the temperature to drop below its adiabatic value. This heat loss is enhanced by the added CO_2 because CO_2 is a strong radiator. The temperatures obtained using the DRM are higher than the ones obtained using the SRM. This is a result of the reabsorption that is accounted for by the DRM. The flame temperature difference realized by using the SRM and DRM increases from 15 to 70 K, as X_{CO_2} increases from 0 to 50%, as CO_2 efficiently emits and absorbs energy. Similar results have been reported by Ju et al. [7].

Comparing the maximum flame temperature calculated under adiabatic conditions and by using the DRM reveals that for $X_{CO_2} < 30\%$, the adiabatic flame temperatures are above the flame temperatures calculated using the of DRM. For $X_{CO_2} > 30\%$, however, the adiabatic calculations result in lower flame temperatures compared to the DRM calculations. This is in agreement with the findings of Ju et al. [7]. This is a result of the preheating of the unburned gas, as it absorbs heat emitted from the broad downstream region of burned gases. It should be noted that the total energy of the system is conserved.

Fig. 14 depicts the temperature profiles of a CH_4/air/CO_2 1D freely-propagating flame with $\phi = 0.7$ and $X_{CO_2} = 50\%$ calculated under adiabatic conditions and by using the SRM and DRM. It can be seen that the temperature of the upstream flow is raised by about 60 K, which is a result of the absorption of the heat that is radiated from the hot burned gases. The optically thick flame indeed has a higher temperature than the adiabatic case inside the flame.

Fig. 15 depicts the laminar flame speeds of flames with $\phi = 0.7$ and X_{CO_2} ranging from 0 to 50% calculated under adiabatic conditions and by using the SRM and DRM. The SRM results in lower laminar flame speeds than the adiabatic ones. This can be contributed to the lower flame temperatures that are caused by the radiative heat loss. However, the differences between these two models are small. For $X_{CO_2} = 0\%$, these two models result in nearly the same laminar flame speed. This is expected as when $X_{CO_2} = 0\%$, the effect of radiation on propagation for a $\phi = 0.7$ methane/air flame is minimum (e.g. [28]).

Comparing the adiabatic and DRM laminar flame speeds, the DRM laminar flame speeds are noticeably higher than the adiabatic values for all X_{CO_2}'s. For the flame with $X_{CO_2} = 50\%$, this is caused by the fact that the DRM results in higher flame temperature compared to the adiabatic value. However, for the $X_{CO_2} = 0\%$ flame, the DRM flame temperature is lower than the adiabatic value. Fig. 16 depicts the adiabatic, SRM, and DRM temperature profiles of the $X_{CO_2} = 0\%$ flame. The DRM does not result in higher temperatures compared to the adiabatic simulations in the flame and postflame region. However, it results in a higher upstream temperature and consequently in higher temperatures at the location at which the main branching reaction $H + O_2 \rightarrow O + OH$ is fully activated; propagation is very sensitive to the forward progress of this reaction.

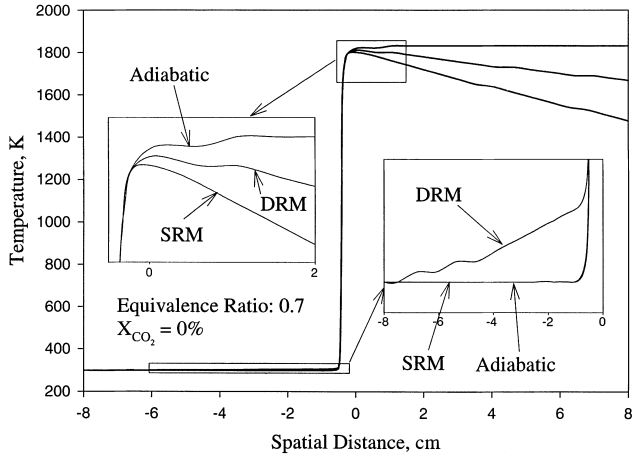

Fig. 16. Temperature profiles of 1D freely-propagating flames, using the adiabatic assumption as well as SRM and DRM.

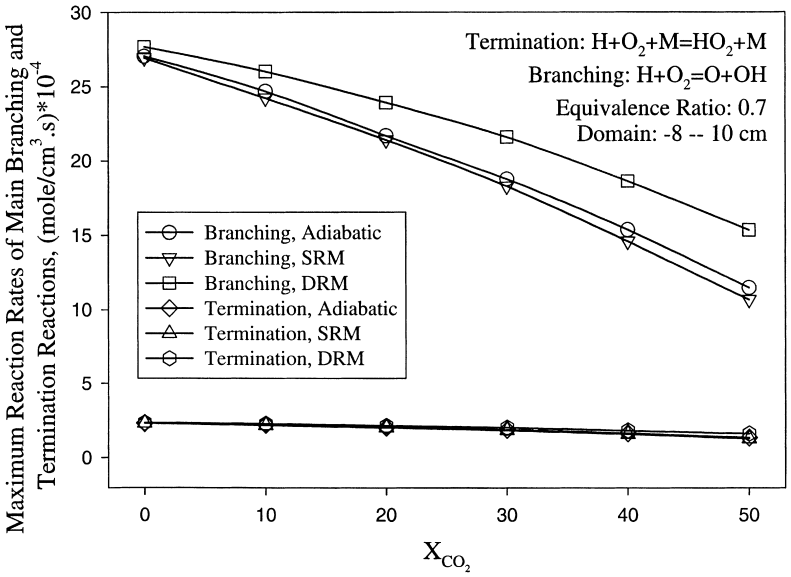

Fig. 17. Maximum reaction rates of the main branching and termination reactions as functions of CO_2 mole fraction in the fuel feed, using the adiabatic assumption, as well as SRM and DRM.

In order to provide further insight into the physics controlling the laminar flame speed, the maximum rates of the main branching ($H + O_2 \rightarrow O + OH$) and the main termination ($H + O_2 + M \rightarrow HO_2 + M$) reactions are plotted in Fig. 17. The dependence of the maximum rate of the main branching reaction on the radiative model used and the X_{CO_2} is nearly identical to that of the laminar flame speeds, as reported in Fig. 15. This observation indicates the strong dependence of the laminar flame speed on the progress of the main branching reaction. This is expected as $H + O_2 \rightarrow O + OH$ is the main radical-producing step, and because of its high activation energy its rate is particularly sensitive to the flame temperature. The main termination reaction rates are one order of magnitude smaller than the main branching reaction rates.

Fig. 18 depicts calculated adiabatic, SRM, and DRM laminar flame speeds as functions of X_{CO_2} for $\phi = 0.6$, 0.7, and 0.8. In all the cases, the SRM values are lower than the adiabatic ones, while the DRM values are higher. The differences between the three models are more profound for lower ϕ's and higher X_{CO_2}'s. The predictions from all the models approach each other as the equivalence ratio increases. This is because radiation heat loss only affects the dynamic response of weak flames, i.e. flames with low ϕ.

From the results reported in Fig. 1, it is apparent that the experimentally measured laminar flame speeds agree well with the predicted ones using the SRM for lean CH_4 flame with X_{CO_2} ranging from 0 to 50%. However, the same results suggest that for flames with high X_{CO_2}'s, the GRI mechanism will not predict laminar flame speeds closely, unless it is optimized by invoking a DRM.

Fig. 19 depicts the effect of radiation on extinction strain rate. As X_{CO_2} increases from 0 to 50%, the calculated

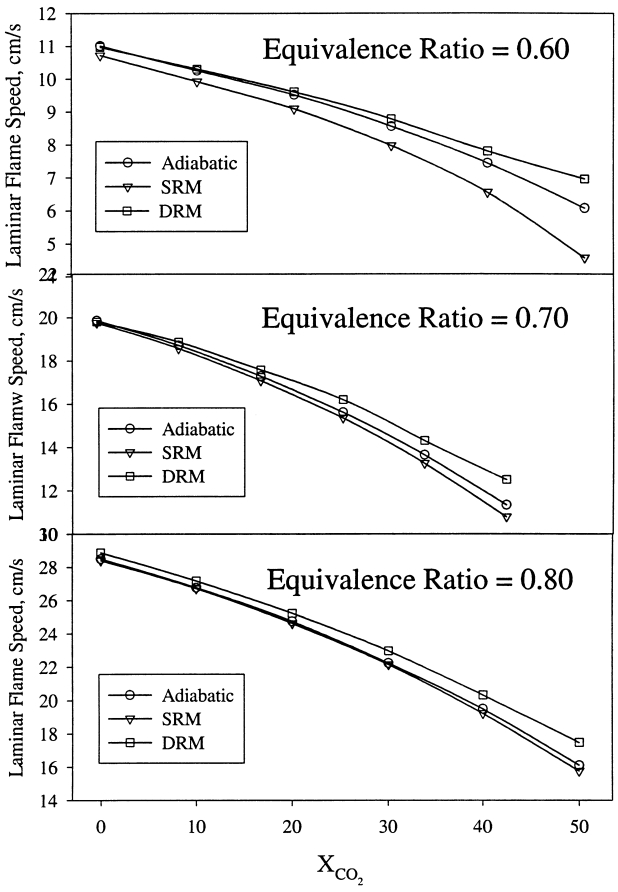

Fig. 18. Laminar flame speeds as functions of CO_2 mole fraction in the fuel feed, using adiabatic assumption as well as SRM and DRM.

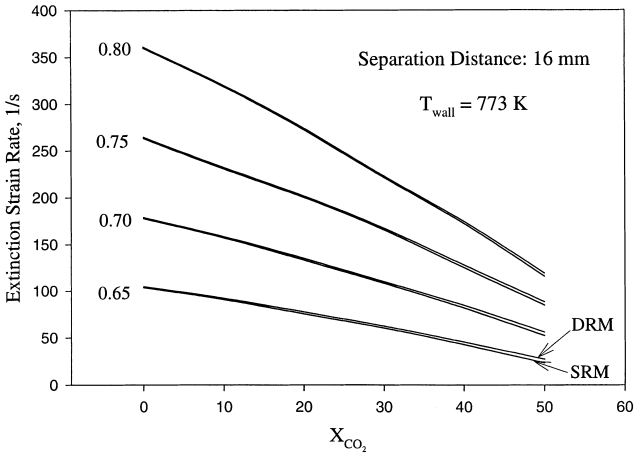

Fig. 19. Variation of numerically determined extinction strain rates with the CO_2 mole fraction in the fuel feed and equivalence ratio, using SRM and DRM.

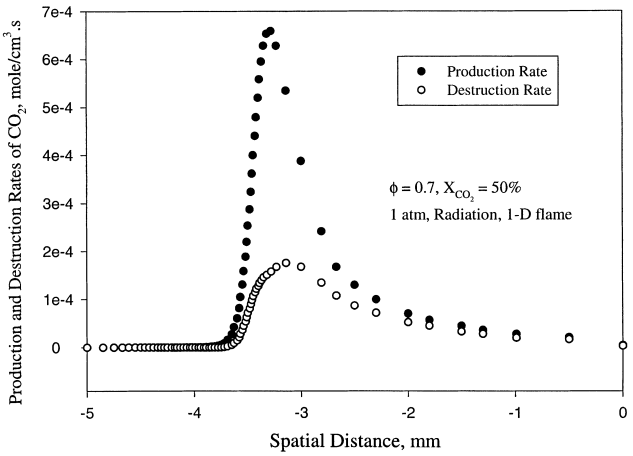

Fig. 20. Spatial variations of numerically determined production and destruction rates of CO_2.

extinction strain rates using DRM exceed those calculated using the optically thin SRM. This is a result of the ability of CO_2 to reabsorb the emitted radiative heat, thus, allowing greater strain rates to be sustained. The difference between SRM and DRM is less profound compared to similar results obtained for laminar flame speeds. This is physically reasonable, as while in the modeling of laminar flame propagation a large spatial domain is considered, the modeling of the strain flames and their extinction behavior includes the use of a finite domain of the order of a centimeter that is identical to the experimental one. As a result, the effect of reabsorption is more profound in the simulation of laminar flame propagation.

4.6. Analysis of the CO_2 effect

The experimental and numerical studies of the various flames have revealed that the presence of CO_2 in the fuel feed has a significant effect on the flame propagation, extinction, and detailed thermal and compositional structures. Such effect of CO_2 can be of kinetic and/or thermal nature. Using the detailed numerical simulations and determining the rates of production and destruction of CO_2 assessed first the kinetic effect. In general, CO_2 is considered as a relatively stable species that can be practically treated as inert. Furthermore, its production in a hydrocarbon flame is chiefly achieved through the main CO oxidation reaction $CO + OH \rightarrow CO_2 + H$. The rates of production and destruction of CO_2 were determined, and are shown in Fig. 20 for a $\phi = 0.7$ flame with $X_{CO_2} = 50\%$. Compared to the production rate, the destruction rate appears to be lower but not negligible. In order to identify the destruction paths of CO_2, an integrated species path analysis was conducted. It was found that CO_2 is mainly consumed through reaction $CH_2(S) + CO_2 \rightarrow CO + CH_2O$; $CH_2(S)$ is the singlet form of CH_2. However, the importance of this reaction on both the flame structure and dynamic response was found to be small, as it plays a minor role to the CH_2O production. Furthermore, its normalized sensitivity on the mass burning rate (laminar flame speed) is low as shown in Fig. 21. As expected (e.g. [13]), the mass burning rate exhibits a significant positive sensitivity on the rates of the main branching $H + O_2 \rightarrow OH + O$ and main CO-consuming $CO + OH \rightarrow CO_2 + H$ reactions. As also expected (e.g. [13]), the mass burning rate exhibits a significant negative sensitivity on the rates of the main termination $H + O_2 + M \rightarrow HO_2 + M$ and HCO-consuming $HCO + O_2 \rightarrow HO_2 + CO$ reactions. Note that the reaction numbers reported in Fig. 21 correspond to those of the GRI 2.11 mechanism.

Based on these observations, the kinetic effect of CO_2 is considered as minor for such small concentrations of CO_2 in the mixture, i.e. less than 5% per mole; recall that X_{CO_2} is the CO_2 mole fraction in the fuel feed rather than the mixture. It should be noted, however, that when CO_2 exists in much greater amounts in the mixture, it could affect the

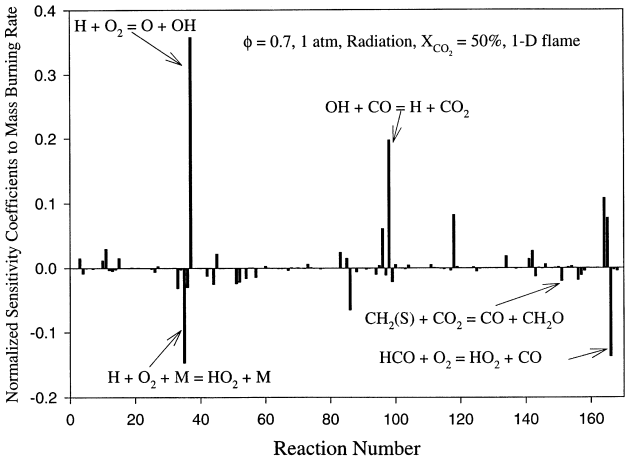

Fig. 21. Normalized sensitivity coefficients of the mass burning rate of 1D freely propagating flame.

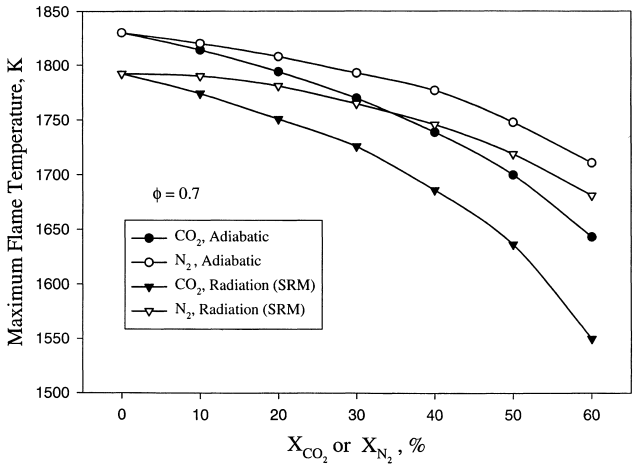

Fig. 22. Numerically determined maximum flame temperatures as functions of CO_2 and N_2 mole fractions in the fuel feed for adiabatic and non-adiabatic flames.

rates of the three-body recombination reactions, as it has augmented third body collision efficiency compared to other abundant species.

The presence of CO_2 can also thermally affect the combustion intensity through two mechanisms. The first mechanism is the reduction of the flame temperature, as CO_2 is, for all practical purposes, an inert and simply acts as a heat sink, thus, diluting the mixture. The second mechanism, as previously discussed, is the radiative heat loss enhancement, as CO_2 efficiently radiates.

The relative importance of those two mechanisms was assessed. Simulations were conducted for both adiabatic and non-adiabatic conditions. Furthermore, in order to compare the effect of adding CO_2 in the fuel feed to the effect of adding equal amounts of N_2, independent simulations were conducted in which N_2 was added to the fuel. The results are shown in Fig. 22. The addition of CO_2 results in a lower flame temperature as compared to N_2 for both adiabatic and non-adiabatic conditions, and this can be trivially attributed to the larger specific heat of CO_2. Comparisons between the adiabatic and non-adiabatic results reveal that the temperature difference between the CO_2-diluted and N_2-diluted cases is larger under non-adiabatic conditions. This demonstrates the radiation enhancement through CO_2 addition, as CO_2 radiates more efficiently compared to N_2.

The effect of radiation enhancements is further illustrated in Fig. 23. The ratio of the calculated non-adiabatic laminar flame speed, $S^o_{u,rad}$, over its adiabatic value, $S^o_{u,adiab}$, is shown as function of ϕ and X_{CO_2}. This ratio is a good measure of the radiation effect on the burning intensity, as the effect of flame temperature through dilution is inherently present in both adiabatic and non-adiabatic simulations. Results show that for the higher X_{CO_2} values, the radiation affects a larger portion of the ϕ-range. For the high value of $X_{CO_2} = 50\%$, radiation starts becoming important even for near-stoichiometric flames. For pure CH_4/air flames, the radiation effect is noticeable for near-limit fuel concentrations, i.e. for $\phi < 0.6$, as also previously observed [28].

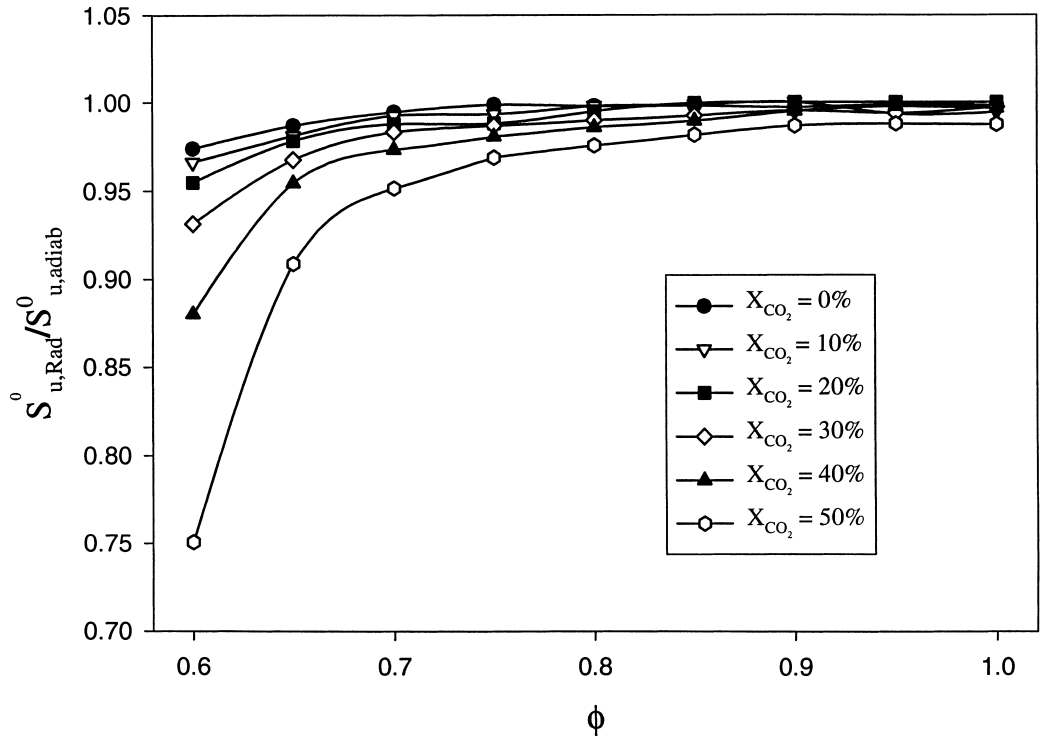

Fig. 23. Effect of radiation on laminar flame speeds of CH_4/CO_2/air mixtures, using SRM.

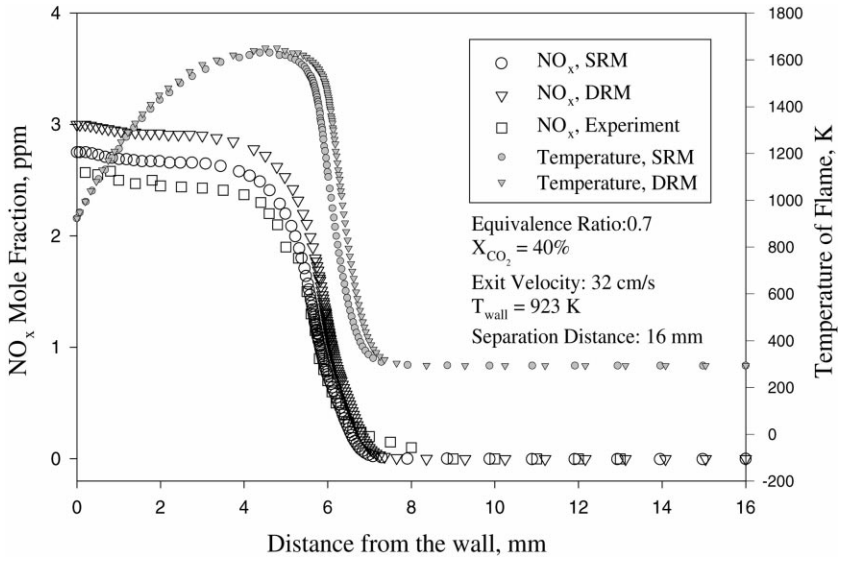

Fig. 24. Experimentally and numerically determined NO_x mole fraction profiles, using SRM and DRM assumptions.

4.7. NO_x emissions

The effect of the presence of CO_2 in the fuel feed on the NO emissions was investigated both numerically and experimentally [35]. Fig. 24, for example, depicts experimental NO_x (i.e. NO + NO_2) measurements conducted along the stagnation streamline together with calculated spatial variations of the NO_x concentrations (in the figure, the temperature profile is used as a marker of the flame zone). The experimental and numerical results agree within 0.5 ppm. The observed minor (in absolute scale) overestimation of the experimental NO_x values may be attributed to uncertainties associated either with the (unavoidable) probe interference and/or with the GRI 2.11 mechanism. The accuracy of the chemiluminescence analyzer is of the order of ppb.

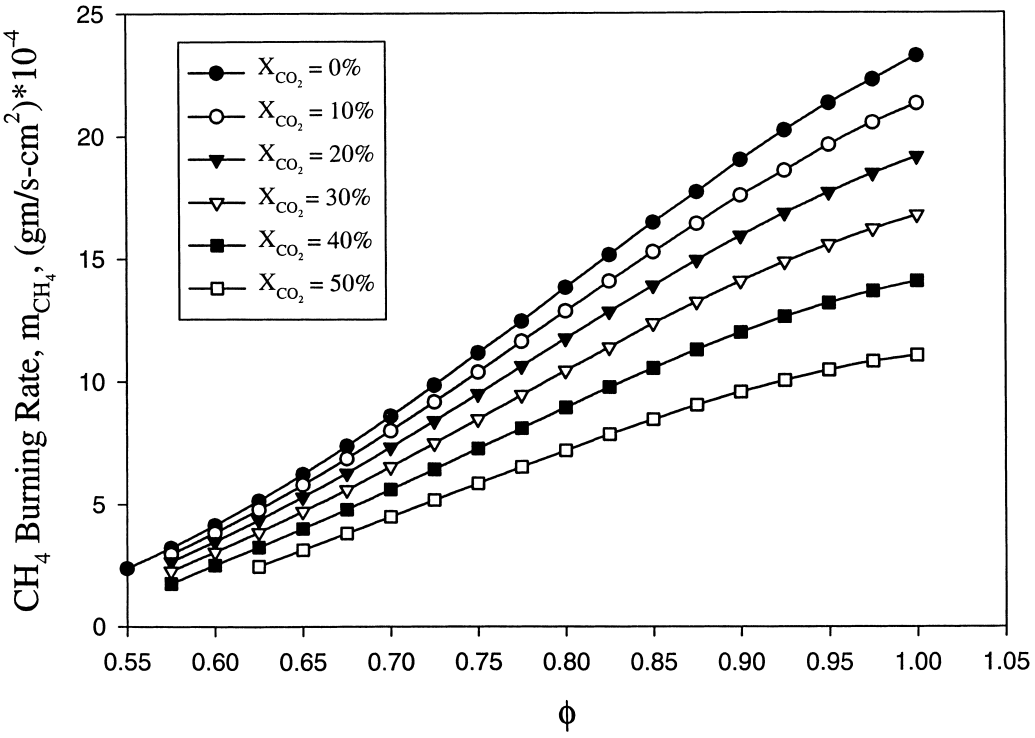

Fig. 25. Variation of the numerically determined CH_4 mass burning rate with the equivalence ratio, ϕ.

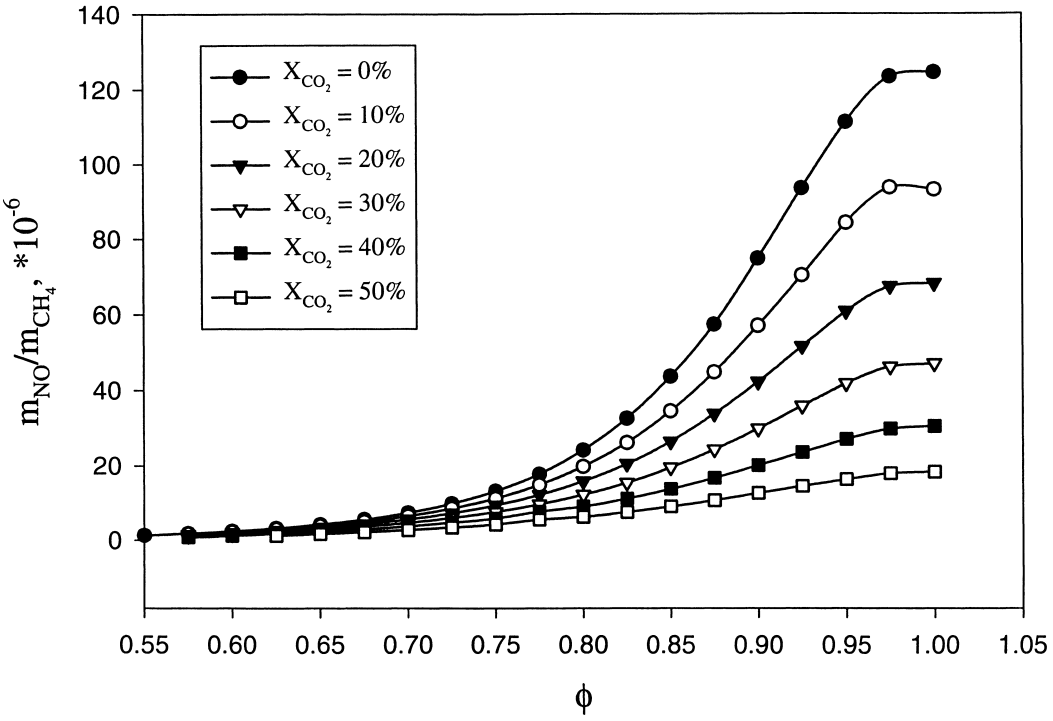

Fig. 26. Variation of the numerically determined NO production per gram of CH_4 consumed with the equivalence ratio, ϕ.

A series of simulations were also conducted for 1D unstrained flames by varying the equivalence ratio from $\phi = 0.55$ to 1.0, and X_{CO_2} from 0 to 50%. From the solution of each flame, the CH_4 burning rate, m_{CH_4}, in g/s cm^2 and the NO mass production rate per gram of consumed CH_4, m_{NO}/m_{CH_4}, were determined. Typical numerical simulation results are shown in Figs. 25 and 26. As expected, it was found that for a fixed X_{CO_2}, both m_{CH_4} and

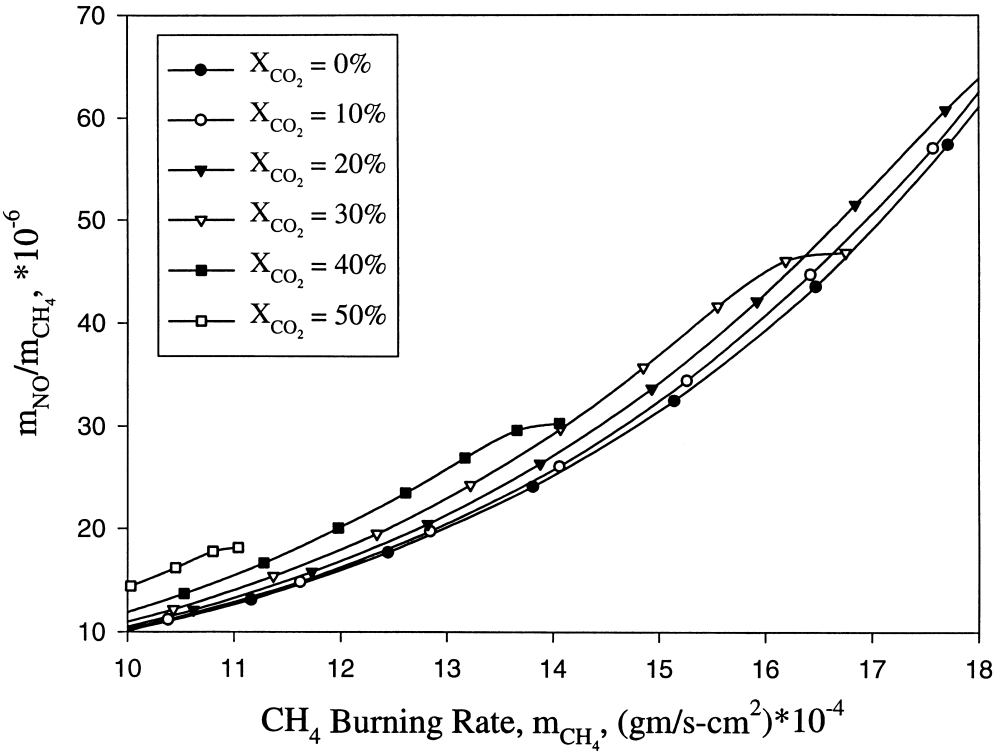

Fig. 27. Variation of the numerically determined NO production per gram of CH_4 consumed with the mass burning rate.

m_{NO}/m_{CH_4} increase with increasing ϕ. This is a result of the increased fuel concentration and flame temperatures. On the other hand, it was found that for a fixed ϕ, both m_{CH_4} and m_{NO}/m_{CH_4} decrease as X_{CO_2} increases. This is, principally, a result of the reduced flame temperature. Interestingly, however, it was found that the emissions of the NO per gram of consumed CH_4 (m_{NO}/m_{CH_4}) are higher for the same m_{CH_4} as X_{CO_2} increases. This is illustrated in Fig. 27. Efforts are currently under way to verify this conclusion experimentally. If validated experimentally, it will be troubling from the perspective of using LFG for energy production.

The mechanisms, which are responsible for such behavior, were also identified using the numerical solutions. In order for two fuel mixtures with different X_{CO_2} to achieve the same m_{CH_4}, the mixture with the higher X_{CO_2} must have higher equivalence ratio, ϕ, or in other words a higher CH_4/O_2 mass/volume ratio. For two flames which are equivalent in that sense, it was found that their flame temperatures are not very different. Under such conditions, the rate of NO production through the thermal and the three-body (i.e. $O + N_2 + M \rightarrow N_2O + M$) mechanisms was found to be of the same order for both fuel mixtures; note that the three-body mechanism is favored for larger X_{CO_2}, as CO_2 is an effective collision partner. However, for the mixture that is characterized by the larger ϕ (corresponding to larger X_{CO_2}), the concentration of the CH-radical is higher compared to the mixture with lower X_{CO_2}. As a result, the prompt mechanism adds to the NO production through the enhancement of the $CH + N_2 \rightarrow HCN + N$ initiation reaction. Thus, for higher X_{CO_2} values, the prompt mechanism contributes to NO production in addition to the thermal and three-body mechanisms, increasing thus the amounts of produced and emitted NO.

5. Conclusions

The combustion characteristics of landfill gas have been experimentally and numerically quantified in the stagnation flow configuration. Laminar flame speeds, extinction strain rates, and detailed flame structures were determined for conditions of relevance to practical combustors. Furthermore, the effect of CO_2 addition to CH_4 on the NO emissions was numerically assessed.

Results indicate that the presence of CO_2 in the fuel feed results in substantial reduction of the laminar flame speeds and extinction strain rates when compared to the pure CH_4 case. This is consistent with the empirical field observations that the use of LFG in practical combustors is associated with substantial stability problems.

The effect of CO_2 on the combustion characteristics was found to be mainly of thermal nature, as the mixture is diluted by the "inert" CO_2 that is also an efficient radiator. Detailed analysis of the numerical flame structures and reaction path analysis reveal that CO_2 is only participating in a reaction with $CH_2(S)$ that, however, has a minor effect on the flame dynamics and structure.

The thermal radiation was calculated by using two models, one using the optically thin assumption and the other accounting for reabsorption and the spectral dependence of the gas emissivity. Results confirmed that as more CO_2 is added, reabsorption becomes important. The experimental results from laminar flame speeds, extinction strain rates, species structures, and thermal structures were compared with the simulation results. The experimental results agree fairly well with the predictions using the optically thin model, but not as well with the predictions using the optically thick model. Accounting for reabsorption was found to result in laminar flame speeds and extinction strain rates that are higher than their adiabatic counterparts. Fundamental flammability limits were also calculated, and it was found that as CO_2 concentration increases, the flammable range noticeably decreases, as expected.

Finally, numerical simulations revealed that the addition of CO_2 increases the NO emissions per gram of CH_4 consumed. Detailed analysis showed that as the CO_2 content in the fuel feed increases, the equivalence ratio that is required to achieve the same rate of CH_4 consumption increases. As the equivalence ratio increases, the NO starts to be produced by the prompt mechanism in addition to the thermal and three-body ones, thus, resulting into larger NO concentrations. This finding suggests that the use of LFG may not be advantageous in terms of NO emissions, and that its combined use with natural gas may be the optimum solution in terms of efficient energy utilization and emissions. Comparisons between experimentally and numerically determined NO concentration profiles revealed that there is a satisfactory agreement, providing thus a validation for the nitrogen kinetics of the GRI 2.11 mechanism.

Acknowledgements

This work was supported by a grant from the California Institute of Energy (CIEE). Useful discussions with Richard Prosser, P.E. of GC Environmental, Inc. and Professor Paul Ronney of USC are gratefully acknowledged.

References

[1] M.G. Robinson, in: Proceedings of D & E Conference on Landfill Gas: Energy & the Environment, Bournemouth, 1990, pp. 551–572.
[2] C. He, D. Herman, R.G. Minet, T.T. Tsotsis, Ind. Eng. Chem. Res. 36 (1997) 4100.
[3] J.T. Haughton, G.J. Jenkins, J.J. Ephraums, Climate Change, The IPPC Scientific Assessment, Cambridge University Press, Cambridge, 1992.
[4] A. Porteous, IEE Proc. A 140 (1993) 86–93.
[5] J.-Y. Ren, W. Qin, F.N. Egolfopoulos, H. Mak, T.T. Tsotsis, Chem. Eng. Sci., 2000, in press.
[6] P.D. Ronney, Proc. Combust. Inst. 22 (1988) 1615–1623.
[7] Y. Ju, G. Masuya, P.D. Ronney, Proc. Combust. Inst. 27 (1998) 2619–2626.

[8] D.L. Zhu, F.N. Egolfopoulos, C.K. Law, Proc. Combust. Inst. 22 (1988) 1537–1545.
[9] B. Karlovitz, D.W. Denniston, D.H. Knapschaefer, F.E. Wells, Proc. Combust. Inst. 4 (1953) 613–620.
[10] C.K. Law, Proc. Combust. Inst. 22 (1988) 1381–1402.
[11] F.N. Egolfopoulos, P. Cho, C.K. Law, Combust. Flame 76 (1989) 375–391.
[12] F.N. Egolfopoulos, C.K. Law, Proc. Combust. Inst. 23 (1990) 333–340.
[13] F.N. Egolfopoulos, D.L. Zhu, C.K. Law, Proc. Combust. Inst. 22 (1990) 471–478.
[14] F.N. Egolfopoulos, H. Zhang, Z. Zhang, Combust. Flame 109 (1997) 237–252.
[15] M.V. Heitor, Prog. Energy Combust. Sci. 19 (1993) 259.
[16] R. Friedman, Proc. Combust. Inst. 4 (1953) 259–263.
[17] J.H. Kent, R.W. Bilger, Proc. Combust. Inst. 14 (1973) 615–625.
[18] F.C. Lockwood, A.D.D. Odidi, Proc. Combust. Inst. 15 (1974) 561–571.
[19] R.W. Bilger, in: B.T. Zinn (Ed.), Progress in Astronautics and Aeronautics, Vol. 53, 1977, p. 44.
[20] F.C. Gouldin, Testing and Measurement Techniques in Heat Transfer and Combustion, AGARD CP-281, 1980.
[21] J.H. Kent, Combust. Flame 24 (1970) 279–281.
[22] M.V. Heitor, A.M.K.P. Taylor, J.H.J. Whitelaw, J. Fluid Mech. 181 (1987) 387.
[23] R.C. Peterson, N.M. Laurendeau, Combust. Flame 60 (1985) 279–284.
[24] F.N. Egolfopoulos, C.S. Campbell, J. Fluid Mech. 318 (1996) 1–29.
[25] R.J. Kee, J.F. Grcar, M.D. Smooke, J.A. Miller, Sandia National Laboratories Report No. SAND85-8240, 1985.
[26] M. Nishioka, C.K. Law, T. Takeno, Combust. Flame 104 (1996) 328–342.
[27] C.K. Law, F.N. Egolfopoulos, Proc. Combust. Inst. 24 (1992) 134–137.
[28] F.N. Egolfopoulos, Proc. Combust. Inst. 25 (1994) 1375–1381.
[29] W.L. Grosshandler, RADCAL: A Narrow-Band Model for Radiation Calculations in a Combustion Environment, NIST Technical Note 1402, 1993.
[30] R.J. Kee, F.M. Rupley, J.A. Miller, Sandia National Laboratories Report No. SAND89-8009, 1989.
[31] R.J. Kee, J. Warnatz, J.A. Miller, Sandia National Laboratories Report No. SAND83-8209, 1983.
[32] C.T. Bowman, M. Frenklach, W.R. Gardiner, G. Smith, The GRI 2.11 Mechanism, 1995, http://www.me.berkeley.edu/gri_mech/.
[33] C.K. Law, F.N. Egolfopoulos, Proc. Combust. Inst. 23 (1990) 1385–1392.
[34] H. Zhang, F.N. Egolfopoulos, Proc. Combust. Inst. 28 (2000), in press.
[35] W. Qin, Experimental and Numerical Study of Combustion of Landfill Gas, Ph.D. Dissertation Thesis, Department of Chemical Engineering, University of Southern California, 2000.